Microscopic models and effective equation of state in nuclear collisions at FAIR energies

L.V. Bravina,[1, *] I. Arsene,[1] J. Bleibel,[2] M. Bleicher,[3] G. Burau,[3] Amand Faessler,[2]
C. Fuchs,[2] M.S. Nilsson,[1] H. Stöcker,[4, †] K. Tywoniuk,[1] and E.E. Zabrodin[1, *]

[1] Department of Physics, University of Oslo, PB 1048 Blindern, N-0316 Oslo, Norway

[2] Institute for Theoretical Physics, University of Tübingen,
Auf der Morgenstelle 14, D-72076 Tübingen, Germany

[3] Institute for Theoretical Physics, University of Frankfurt,
Max-von-Laue-Str. 1, D-60438 Frankfurt a.M., Germany

[4] Gesellschaft für Schwerionenforschung mbH, Planckstraße 1, D-64291 Darmstadt, Germany

(Dated: April 9, 2008)

Two microscopic models, UrQMD and QGSM, were employed to study the formation of locally equilibrated hot and dense nuclear matter in heavy-ion collisions at energies from $11.6A$ GeV to $160A$ GeV. Analysis was performed for the fixed central cubic cell of volume $V = 125\,\mathrm{fm}^3$ and for the expanding cell which followed the growth of the central area with uniformly distributed energy. To decide whether or not the equilibrium was reached, results of the microscopic calculations were compared to that of the statistical thermal model. Both dynamical models indicate that the state of kinetic, thermal and chemical equilibrium is nearly approached at any bombarding energy after a certain relaxation period. The higher the energy, the shorter the relaxation time. Equation of state has a simple linear dependence $P = a(\sqrt{s})\varepsilon$, where $a \equiv c_s^2$ is the sound velocity squared. It varies from 0.12 ± 0.01 at $E_{lab} = 11.6A$ GeV to 0.145 ± 0.005 at $E_{lab} = 160A$ GeV. Change of the slope in $a(\sqrt{s})$ behavior occurs at $E_{lab} = 40A$ GeV and can be assigned to the transition from baryon-rich to meson-dominated matter. The phase diagrams in the $T - \mu_B$ plane show the presence of kinks along the lines of constant entropy per baryon. These kinks are linked to the inelastic (i.e. chemical) freeze-out in the system.

PACS numbers: 25.75.-q, 24.10.Lx, 24.10.Pa, 64.30.-t

I.   INTRODUCTION

Experiments on heavy-ion collisions carried out for the last two decades at GSI's Schwerionen Synchrotron (SIS), LBL's Bevalac, CERN's Super Proton Synchrotron (SPS), BNL's Alternating Gradient Synchrotron (AGS) and Relativistic Heavy Ion Collider (RHIC) have significantly helped us in understanding of properties of hot and dense nuclear matter. The collisions at top RHIC energy $\sqrt{s} = 200A$ GeV or at energy of coming soon CERN's Large Hadron Collider (LHC) $\sqrt{s} = 5.5A$ TeV probe the domain of high temperatures and low net baryon densities, while the systems with lower temperatures but with much higher baryon densities should be produced in heavy-ion collisions at relatively moderate energies around $E_{lab} = 30A$ GeV accessible for future GSI's Facility for Antiproton and Ion Research (FAIR) accelerator [1]. Most likely, the matter under such extreme conditions is composed of partons, i.e. quarks and gluons, in the phase of quark-gluon plasma (QGP), colored tubes of

chromo-electric field (or strings), hadrons and their resonances. The question about the equation of state (EOS) of such substance remains still open. Present status of the nuclear phase diagram in terms of temperature T and baryon chemical potential μ_B is sketched in Fig. 1. The
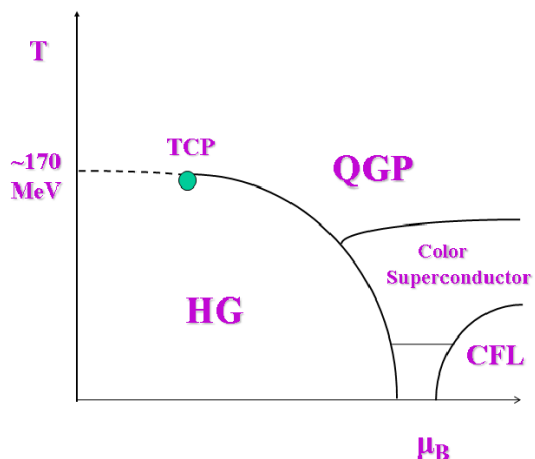

FIG. 1: (Color online) Present status of nuclear phase diagram in the $T - \mu_B$ plane.

highly anticipated transition between the hot hadron gas (HG) and the QGP is of first order for relatively dense baryonic substances only. With rising temperature and

*Also at Skobeltzyn Institute for Nuclear Physics, Moscow State University, RU-119899 Moscow, Russia

†Also at Frankfurt Institute for Advanced Studies (FIAS), University of Frankfurt, Max-von-Laue-Str. 1, D-60438 Frankfurt a.M., Germany

dropping baryon density and chemical potential the transition becomes of second order at the so-called tricritical point (TCP). After that it is transformed to a smooth crossover [2]. Although the theory cannot localize the position of the TCP on T-μ_B plane, lattice quantum chromodynamic (LQCD) calculations indicate that it might be somewhere between the points with $T \approx 160\,\mathrm{MeV}$ and $\mu_B = 360\,\mathrm{MeV}$ [3] or $\mu_B = 470\,\mathrm{MeV}$ [4]. These values are close to the chemical freeze-out parameters obtained from the analysis of heavy-ion collisions at energies between $E_{lab} = 11.6A$ GeV and $E_{lab} = 40A$ GeV within the statistical models [5, 6, 7]. They are close also to the temperatures and baryon chemical potentials in the central zone of heavy-ion reactions generated by microscopic transport models [8, 9, 10, 11, 12]. Another interesting feature of the collisions at bombarding energies around $40A$ GeV is the transition from baryon-dominated matter to meson-dominated one. According to microscopic models, in gold-gold collisions at top AGS energy nearly 70% of total energy is deposited in baryonic sector. At top SPS energy mesons are carrying 70% of the total energy, and at $E_{lab} \approx 40A$ GeV the energy parts of mesons and baryons are roughly the same. - The particle composition is changing. Is it possible to trace consequences of this change in microscopic model analysis? To answer this question two transport Monte Carlo models were employed: ultrarelativistic quantum molecular dynamics (UrQMD) model [13] and quark-gluon string model (QGSM) [14]. The models use different mechanisms of string excitation and fragmentation. UrQMD relies on the longitudinal excitation, while the color exchange scheme is employed in QGSM. Central gold-gold collisions with zero impact parameter $b = 0$ fm were simulated at bombarding energies $E_{lab} = 11.6, 20, 30, 40, 80$ and $160A$ GeV, respectively. Microscopic parameters related to quantities conserved in strong interactions, namely, the total energy, the net baryon charge, and the net strangeness extracted for a certain volume of the reaction were inserted into a system of nonlinear equations to obtain temperature, baryon chemical potential and strangeness chemical potential of an ideal hadron gas in equilibrium. If the yields and transverse momentum spectra of particles obtained in microscopic simulations are close to that provided by the statistical model, the matter in the cell is considered to be in the vicinity of equilibrium. Then its equation of state and other thermodynamic characteristics can be derived and studied.

Relaxation of hot matter to equilibrium in the central cell of central heavy-ion collisions has been studied within the UrQMD model in [8, 9, 10, 11, 12] for energies ranging from $11.6A$ GeV at AGS to $\sqrt{s} = 200A$ GeV at RHIC, and, partially, within the QGSM [15, 16]. The size of the cell once chosen has been fixed throughout the system evolution. In the present paper we modify the analysis of the early stage in order to trace the expansion of an initially small area of homogeneity just after its formation. The central volume was further sub-separated into smaller cells embedded within each other ("matryoshka-

doll" structure). The transition of analysis from the smaller cell to the larger one was allowed if, and only if, the energy densities in both cells were the same. Regardless of the microscopic model applied for the actual calculations, the formation of (quasi)equilibrated state in the central cell at all bombarding energies in question is observed. The matter in the cell expands isentropically with constant entropy-per-baryon ratio. The isentropic regime arises even before the chemical and thermal equilibration takes place. Due to coarse-graining of the central volume characteristic kinks in the temperature vs. baryochemical potential phase diagrams are found for both model simulations. This feature has not been seen in the previous studies because of the averaging of energy and baryon densities, in fact non-isotropically distributed within the relatively large volume.

The paper is organized as follows. Similarities and differences of the microscopic string models chosen for the analysis are discussed in Sect. II. In Sect. III criteria of thermal and chemical equilibrium are formulated, and Sect. IV describes the statistical model of an ideal hadron gas used for the comparison with both microscopic models. Section V presents the model study of the relaxation process in the cells with fixed and variable volumes. Special interest is paid to collisions at $E_{lab} = 20A$ GeV and $40A$ GeV, and obtained results are compared to that at neighbor energies. Conclusions are drawn in Sect. VI.

II. FEATURES OF URQMD AND QGSM

A. Similarities of the microscopic models

Both UrQMD and QGSM are formulated as Monte-Carlo event generators allowing to perform a careful analysis of the measurable quantities by introducing all necessary experimental cuts. The models are designed to describe hadronic, hadron-nucleus, and nuclear collisions in a broad energy range. In the hadronic sector both models treat the production of new particles via formation and fragmentation of specific colored objects, strings. Strings are uniformly stretched, with constant string tension $\kappa \approx 1\,\mathrm{GeV/fm}$, between the quarks, diquarks and their antistates. The excited string is fragmenting into pieces via the Schwinger-like mechanism of $q\bar{q}$ and $qq - \bar{q}\bar{q}$ pair production, and the produced hadrons are uniformly distributed in the rapidity space.

To describe hadron-nucleus (hA) and nucleus-nucleus ($A+A$) collisions the momenta and positions of nucleons in the nuclei are generated according to the Fermi momentum distribution and the Wood-Saxon density distribution, respectively. The black disk approximation is adopted as criterion of interaction. It means that two hadrons can interact both elastically and inelastically if the distance d between them is smaller than $\sqrt{\sigma/\pi}$, where σ is the total cross section. Tables of the experimentally available information, such as hadron cross sections, resonance widths and decay modes, are imple-

mented in the models. If this information is lacking, the one-boson exchange model, detailed balance considerations and isospin symmetry conditions are employed. The propagation of particles is governed by Hamilton equation of motion, and both models use the concept of hadronic cascade for the description of hA and $A + A$ interactions. Note that such a rescattering procedure is very important in the case of relativistic heavy-ion collisions and is necessary for the thermalization of the fireball. Due to the uncertainty principle newly produced particles can interact further only after a certain *formation time*. However, hadrons containing the valence quarks can interact immediately with the reduced cross section $\sigma = \sigma_{qN}$. The Pauli principle is taken into account via the blocking of the final state, if the outgoing phase space is occupied. The Bose enhancement effects are not implemented yet.

B. Differences between the microscopic models

The differences between the models for hadronic interactions arise on three stages. First stage is the formation of strings. The UrQMD belongs to group of models based on classical FRITIOF model [17], while the QGSM uses the Gribov Reggeon field theory (RFT) [18, 19]. In the FRITIOF model the longitudinal excitation of strings is employed, and the string masses arise from momentum transfer. In the Gribov-Regge models the string masses appear due to the color exchange mechanism, and strings are stretching between the constituents belonging to different hadrons. Longitudinal excitation of strings is also possible in the QGSM. This mechanism describes the processes of single and double diffraction. The second stage concerns the string fragmentation. The Lund JET-SET routine [20], used in the UrQMD, assumes that the string always breaks into a sub-string and a particle on a mass shell. In the QGSM the Field-Feynman algorithm [21] with independent jets is applied. Therefore, the fragmentation functions which determine the energy, momentum, and the type of the hadrons produced during the string decay, are different in the models. The third stage deals with the number and type of the stings produced in the collision. Due to the different mechanisms of string excitation and fragmentation, these numbers are also different for two microscopic models in question. Last but not least, both models do not use the same tables of hadrons, chosen as discrete degrees of freedom. Whereas the UrQMD contains 55 baryon and 32 meson states together with their antistates, the QGSM takes into account octet and decuplet baryons, and nonets of vector and pseudoscalar mesons, as well as their antiparticles. Further details can be found in [13] and [14]. Recently, the QGSM has been extended by the implementation of a parton recombination mechanism [16]. Since parton recombination plays a minor role for nuclear collisions at intermediate energies, the whole analysis of the relaxation process is done for the standard QGSM. We see

that the basic underlying principles and designs of the models are quite far from each other. By using both the UrQMD and QGSM for studies of the relaxation process in a broad energy range one can expect that the model-dependent effects, caused by application of a particular event generator, will be significantly reduced.

III. STATISTICAL MODEL OF AN IDEAL HADRON GAS

For our analysis of the thermodynamic conditions in the cell we use a conventional statistical model (SM) of an ideal hadron gas formulated in pioneering works of Fermi [22] and Landau [23]. The statistical approach was successfully applied to the description of particle production in heavy-ion collisions from AGS to RHIC energies (see [6] and references therein). In chemical and thermal equilibrium the distribution functions of hadron species i at temperature T read (in units of $c = k_B = \hbar = 1$)

$$f(p, m_i) = \left[\exp\left(\frac{\epsilon_i - \mu_i}{T}\right) \pm 1\right]^{-1} , \quad (1)$$

where p, m_i, $\epsilon_i = \sqrt{p^2 + m_i^2}$, and μ_i are the full momentum, mass, energy, and the total chemical potential of the hadron, respectively. The "+" sign is for fermions and the "−" sign for bosons. Since in equilibrium the chemical potentials associated to nonconserved charges vanish, the total chemical potential assigned to the i-th hadron is a linear combination of its baryon chemical potential μ_B and strangeness chemical potential μ_S

$$\mu_i = B_i \mu_B + S_i \mu_S , \quad (2)$$

with B_i and S_i being the baryon charge and the strangeness of the particle, respectively. The isospin chemical potential (or, alternatively, chemical potential associated with electric charge) is usually an order of magnitude weaker than μ_B and μ_S. Therefore, the dependence on this potential is disregarded in Eq. (2). Then, particle number density n_i and energy density ε_i are simply moments of the distribution function

$$n_i = \frac{g_i}{(2\pi)^3} \int f(p, m_i) d^3p , \quad (3)$$

$$\varepsilon_i = \frac{g_i}{(2\pi)^3} \int \sqrt{p^2 + m_i^2} f(p, m_i) d^3p , \quad (4)$$

with g_i being the spin-isospin degeneracy factor of hadron i. The partial hadron pressure given by the statistical model reads

$$P_i = \frac{g_i}{(2\pi)^3} \int \frac{p^2}{3(p^2 + m_i^2)^{1/2}} f(p, m_i) d^3p . \quad (5)$$

The integrals in Eqs. (3)−(5) can be calculated numerically. Another way is to use a series expansion of Eq. (1)

in the form [23]

$$f(p, m_i) = \sum_{n=1}^{\infty} (\mp 1)^{n+1} \exp\left(-n\frac{E_i - \mu_i}{T}\right) , \quad (6)$$

which is inserted into Eqs. (3)−(5). After some straightforward calculations one gets

$$n_i = \frac{g_i m_i^2 T}{2\pi^2} \sum_{n=1}^{\infty} \frac{(\mp 1)^{n+1}}{n} \exp\left(\frac{n\mu_i}{T}\right) K_2\left(\frac{nm_i}{T}\right) , (7)$$

$$\varepsilon_i = \frac{g_i m_i^2 T^2}{2\pi^2} \sum_{n=1}^{\infty} \frac{(\mp 1)^{n+1}}{n^2} \exp\left(\frac{n\mu_i}{T}\right)$$
$$\times \left[3K_2\left(\frac{nm_i}{T}\right) + \frac{nm_i}{T}K_1\left(\frac{nm_i}{T}\right)\right] , \quad (8)$$

$$P_i = \frac{g_i m_i^2 T^2}{2\pi^2} \sum_{n=1}^{\infty} \frac{(\mp 1)^{n+1}}{n^2} \exp\left(\frac{n\mu_i}{T}\right) K_2\left(\frac{nm_i}{T}\right) (9)$$

where K_1 and K_2 are modified Hankel functions of first and second order, respectively. The first terms in Eqs. (7)−(9) correspond to the case of Maxwell-Boltzmann statistics, which neglects the ± 1 term in particle distribution function (1).

The entropy density in the cell is represented by a sum over all particles of the product $f(p, m_i)[1 - \ln f(p, m_i)]$ integrated over all possible momentum states

$$s = -\sum_i \frac{g_i}{2\pi^2} \int_0^{\infty} f(p, m_i) [\ln f(p, m_i) - 1] \, p^2 dp. \quad (10)$$

According to the presented formalism, the hadron composition and energy spectra in equilibrium are determined by just three parameters, namely, the temperature, the baryon chemical potential, and the strangeness chemical potential. In order to define values of T, $\mu_{\rm B}$, and $\mu_{\rm S}$ one has to obtain the total energy density ε, baryon density $\rho_{\rm B}$ and strangeness density $\rho_{\rm S}$ for a given volume from microscopic model calculations, and insert them as input parameters into the system of nonlinear equations

$$\rho_B = \sum_i B_i \, n_i(T, \mu_{\rm B}, \mu_{\rm S}) , \quad (11)$$

$$\rho_S = \sum_i S_i \, n_i(T, \mu_{\rm B}, \mu_{\rm S}) , \quad (12)$$

$$\varepsilon = \sum_i \varepsilon_i(T, \mu_{\rm B}, \mu_{\rm S}) , \quad (13)$$

where $n_i(T, \mu_{\rm B}, \mu_{\rm S})$ and $\varepsilon_i(T, \mu_{\rm B}, \mu_{\rm S})$ are given by Eqs. (3)-(4). Since the particle data tables implemented in the microscopic models contain different numbers of hadrons, two versions of the SM with properly adjusted lists of hadron species are used, i.e. the number of hadronic degrees of freedom in the macroscopic model should correspond to that in the microscopic model. To decide whether or not the equilibrium is reached the criteria of the equilibrated state for open systems, discussed in the next section, should be applied.

IV. CRITERIA OF THERMAL AND CHEMICAL EQUILIBRIUM

Criteria of local equilibrium for open systems were formulated in [9], and we recall them briefly. Compared to a nonequilibrium state, the equilibrium is characterized by the absence of collective effects, like flow of matter or flow of energy. The fireball produced in heavy-ion collisions is always expanding both radially and longitudinally. Therefore, the centrally placed symmetric cell is chosen to diminish effects caused by nonzero collective velocity of any asymmetric or asymmetrically located cell. The cell should be neither too small to allow for the statistical treatment, nor too large, - otherwise the homogeneous distribution of matter may not be reached. Previous studies [8, 9, 10, 11, 15] found that the cubic cell of volume $V = 125$ fm^3 centered around the center-of-mass of colliding gold-gold or lead-lead nuclei is well suited for such an analysis. Clearly, the relaxation to local equilibrium cannot occur earlier than at a certain time needed for the Lorentz contracted nuclei to pass through each other and leave the cell

$$t^{eq} \geq \frac{2R}{\gamma\beta} + \frac{\Delta z}{2\beta} . \quad (14)$$

Here R is the nuclear radius, Δz is the cell length in longitudinal direction, β is the velocity of nuclei in the c.m. frame, and $\gamma = (1 - \beta^2)^{-1/2}$. Quite unexpectedly, the reduction of the longitudinal size of the cell from 5 fm to 1 fm does not automatically imply a faster equilibration in the smaller cell: the transition times are practically the same [10]. This means that the transition to equilibrium takes place simultaneously within a relatively large volume along the beam axis.

Isotropy of the pressure gradients is a necessary condition for kinetic equilibration. Diagonal elements of the pressure tensor $P_{\{x,y,z\}}$ are calculated from the virial theorem [24]

$$P_{\{x,y,z\}} = \frac{1}{3V} \sum_{i=h} \frac{p_{i\{x,y,z\}}^2}{(m_i^2 + p_i^2)^{1/2}} , \quad (15)$$

where V, m_i and p_i are the volume of the cell, the mass and the momentum of the ith hadron, respectively. Figure 2 depicts the convergence of the transverse pressure in the cell to the longitudinal one in the UrQMD and the QGSM calculations. Both models claim that the pressure becomes isotropic at $t \leq 10$ fm/c after beginning of the collision. The time of convergence decreases with rising bombarding energy. The pressure calculated according to the statistical model is plotted onto the results of microscopic simulations also. The agreement between microscopic and macroscopic calculations is good for a period of about $t = 8 - 10$ fm/c. Then the matter in the cell becomes quite dilute, and the collision rate is not sufficiently high to maintain equilibrium anymore. However, the isotropy of pressure can be obtained, for instance, in
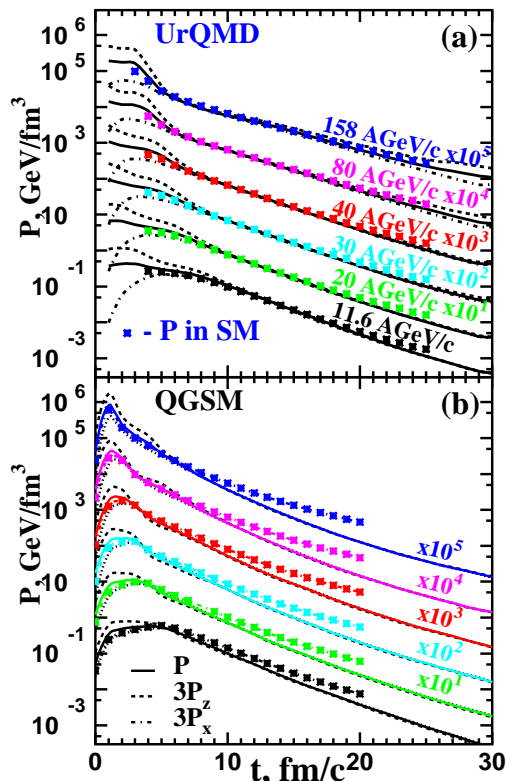
FIG. 2: (Color online) The longitudinal ($3P_z$, dashed curves) and the transverse ($3P_x$, dash-dotted curves) diagonal components of the microscopic pressure tensor in the central 125 fm^3 cell in (a) UrQMD and (b) QGSM calculations of central Au+Au collisions at energies from $11.6A$ GeV to $158A$ GeV. Asterisks indicate the pressure given by the statistical model and solid lines show the total microscopic pressure.

a spherically expanding system of non-interacting particles. To exclude such a situation from the analysis one has to impose two additional criteria concerning thermal and chemical equilibrium.

For a closed system in equilibrium the distribution functions of particles are given by Eq. (1) with an unique temperature, so the hadron composition and energy spectra are fixed. In open systems neither the energy density nor the number of particles is conserved. Therefore, the snapshots of hadron abundances and energy spectra obtained at a certain time t should be compared with those corresponding to an ideal gas in equilibrium. The technical procedure is simple. At the very beginning, the pressure gradients in transverse and longitudinal directions are considered. If the pressure isotropy is restored, say, within 10%-limit of accuracy, the densities of conserved quantities, i.e. energy, baryon charge, and strangeness, determined microscopically, (i) should be used as an input to Eqs. (11)-(13). The solution of this system of equations (ii) provides us with values of the temperature, baryon chemical potential, and strangeness chemical potential which fully determine the composition and spectra of particles. By (iii) a comparison of microscopic

and macroscopic yields of the most abundant hadronic species one can decide whether or not the chemical equilibrium occurs, whereas (iv) the energy spectra of these hadrons should possess a common slope corresponding to $1/T$ (thermal equilibrium). The similarity of the particle distributions means that our system is in the vicinity of equilibrium. At each subsequent time step the procedure described by (i)-(iv) is repeated.

V. RELAXATION TO EQUILIBRIUM. RESULTS AND DISCUSSION

A. Yields and energy spectra

The yields of main hadron species, i.e. $N, \Delta, \Lambda + \Sigma, \pi, K$ and $\overline{K}$ in the central cell are shown in Fig. 3 for central Au+Au collisions at $E_{lab} = 40A$ GeV. For all particles, except pions, the agreement between the microscopic and macroscopic estimates at $t \geq 9$ fm/c is good. Compared to the microscopic models, the number of pions is underestimated in the SM. The pion excess comes from the many-body decaying resonances, such as $N^*, \Delta^*, \Lambda^*, \omega$, etc, and strings. After $t = 10 - 13$ fm/c the many-body processes play just a minor role, and the pion multiplicity slowly converges to the equilibrium value. It looks like all species of the hadronic cocktail, except pions, are not far from the chemical equilibrium. It is well-known that the pure statistical model of an ideal hadron gas, which does not include effective chemical potential for pions or weak decays, systematically underestimates the pion yields compared to experimental data. Nevertheless, the excess of pions in the model with short table of resonances, QGSM, is quite significant. This circumstance should affect the thermal spectra of all hadrons, provided the thermalization is reached.

To verify how good the temperature is reproduced, the energy spectra $dN/4\pi\rho EdE$ are displayed in Fig. 4. The Boltzmann fit to particle distributions is performed, and the SM calculations are plotted onto the microscopic results also. Both in UrQMD and in QGSM the energy spectra agree well with the exponential form of the Boltzmann distributions. Despite the good quality of the fit, the abundance of pions in particle spectrum leads to significant reduction of the effective temperature of the system within the QGSM calculations. Analytical estimates of the temperature drop (see *Appendix* A) are close to the temperatures extracted from the fit. It would be possible to diminish the pion yield by taking into account larger part of the resonance states, but our intention is to check the principal occurrence of the (quasi)equilibrium states in different microscopic models and to define the limits imposed on the effective equation of state. Note also, that significant part of the pion spectrum seems to be softer compared to other hadronic species. These pions are coming mainly from the decays of resonances and experience too few elastic collisions, that are necessary for their thermalization. Since the hadronic matter in
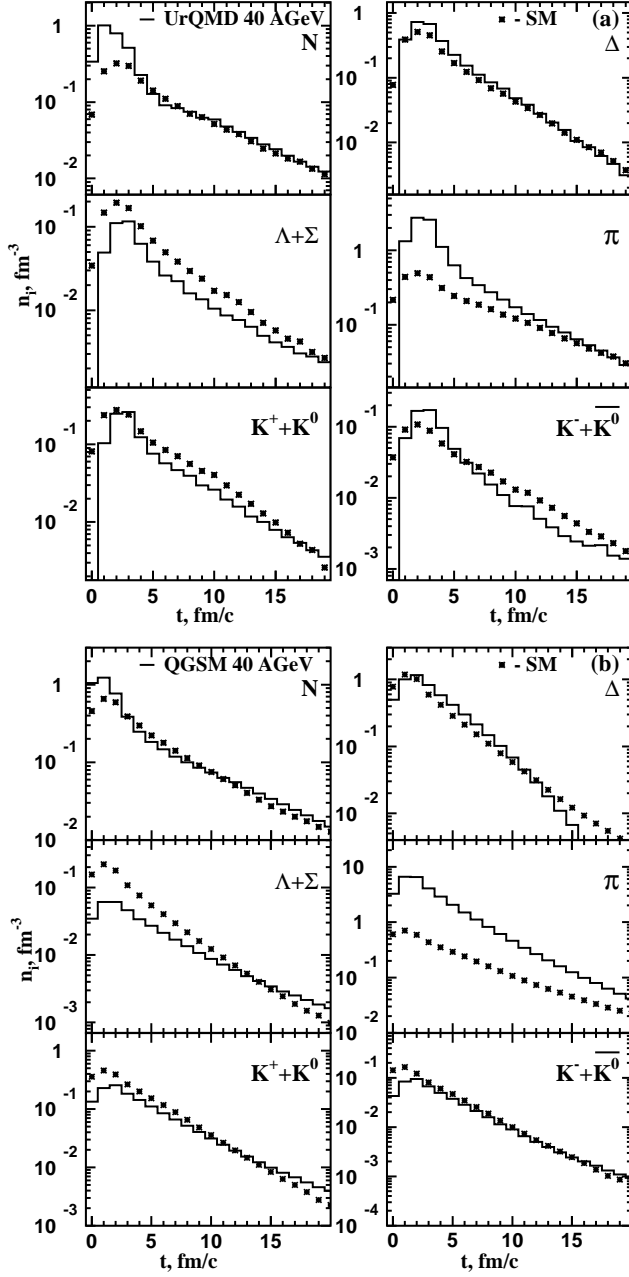
FIG. 3: Evolution of yields of hadron species in the central cell of volume $V = 125\,\text{fm}^3$ in (a) UrQMD and (b) QGSM calculations (histograms) of central Au+Au collisions at $40A$ GeV. Asterisks denote the results of the statistical model.

the central cell reaches the state of thermal equilibrium, one can apply the mathematical apparatus formulated in Sect. III and, finally, obtain the anticipated EOS.

B. Evolution of the cell characteristics

According to the information provided by Figs. 2 - 4, the appropriate time to start the study of thermodynamic
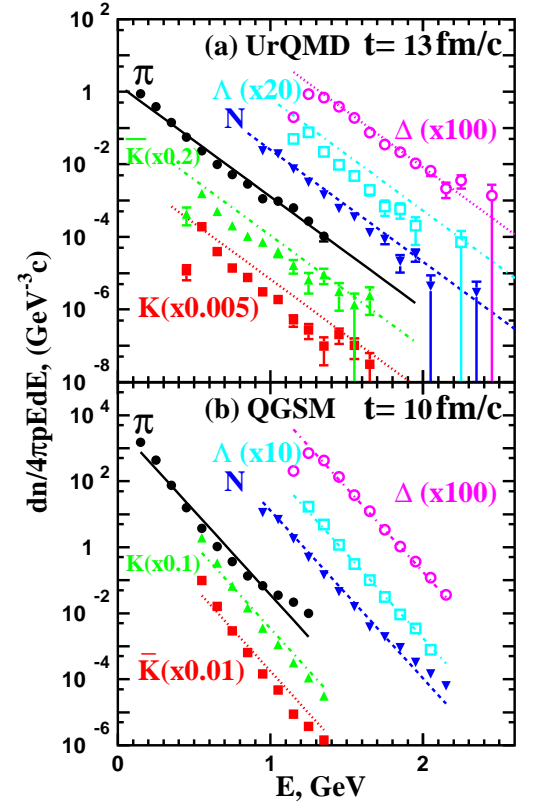

FIG. 4:   (Color online) Energy spectra of N ($\blacktriangledown$), Λ ($\square$), π ($\bullet$), $\overline{K}$ ($\blacktriangle$), K ($\blacksquare$), and Δ ($\bigcirc$) in the central 125 fm^3 cell in (a) UrQMD and (b) QGSM calculations of central Au+Au collisions at $40A$ GeV at $t = 13\,\text{fm}/c$ and $t = 10\,\text{fm}/c$, respectively. Lines show the results of the fit to Boltzmann distribution.

conditions in the cell is $t = 11\,\text{fm}/c$ for the reactions at $E_{lab} = 20A$ GeV and $t = 9\,\text{fm}/c$ for $E_{lab} = 40A$ GeV. The input parameters obtained in the microscopic model analysis are listed in Tables I-II together with the output thermodynamic characteristics given by the SM. Because of the different number of hadronic states employed by QGSM and UrQMD, the tables of available hadronic degrees of freedom in the statistical model are adjusted properly. The only objects not taken into account in the SM are strings. The detailed analysis done in [25, 26] shows that string processes play only a minor role at such late times in the central part of the reaction. Less than 5% of the total amount of hadronic collisions result to formation of strings. The strings produced at late time stages are quite light, and usually just one extra-particle, most commonly a pion, is produced after the string fragmentation. This circumstance, however, may account for the pion overproduction (see Fig. 3), since the inverse reactions such as 3(or more)→2 are not incorporated in the employed versions of both microscopic models.

For both energies the baryon density in the cell at the beginning of the equilibrium phase is about 30% larger than the normal baryon density $\rho_0 = 0.16\,\text{fm}^{-3}$ in the UrQMD calculations. Whereas QGSM allows for the

TABLE I: The time evolution of the thermodynamic characteristics of hadronic matter in the central cell of volume $V = 125$ fm^3 in central Au+Au collisions at bombarding energy $20A$ GeV. The temperature, T, baryochemical potential, μ_B, strange chemical potential, μ_S, pressure, P, entropy density, s, and entropy density per baryon, s/ρ_B, are extracted from the statistical model of ideal hadron gas, using the microscopically evaluated energy density, ε^{cell}, baryonic density, ρ_B^{cell}, and strangeness density, ρ_S^{cell}, as input. Of each pair of numbers, the upper one corresponds to the UrQMD calculations, and the lower one to the QGSM calculations.

Time	ε^{cell}	ρ_B^{cell}	ρ_S^{cell}	T	μ_B	μ_S	P	s	s/ρ_B^{cell}
fm/c	MeV/fm^3	fm^{-3}	fm^{-3}	MeV	MeV	MeV	MeV/fm^3	fm^{-3}	
11	464.2	0.210	-0.0143	144.5	450.5	92.7	59.6	2.97	14.16
	522.6	0.257	-0.0059	150.2	487.8	116.1	73.8	3.13	12.19
12	343.2	0.160	-0.0115	137.9	459.2	86.4	44.0	2.27	14.18
	385.7	0.197	-0.0051	141.9	498.1	109.4	53.1	2.40	12.16
13	255.2	0.124	-0.0093	131.5	469.5	80.4	32.6	1.75	14.15
	286.9	0.153	-0.0046	134.0	609.5	103.1	38.5	1.85	12.09
14	189.9	0.096	-0.0072	124.9	481.7	75.8	24.1	1.34	14.06
	214.2	0.117	-0.0035	127.2	515.9	97.1	28.2	1.43	12.22
15	143.9	0.075	-0.0064	119.2	492.8	68.6	18.1	1.05	13.97
	162.3	0.091	-0.0028	121.0	522.3	91.5	20.1	1.12	12.35
16	108.8	0.059	-0.0052	113.7	502.5	62.7	13.6	0.82	13.97
	125.4	0.072	-0.0025	115.4	529.2	85.4	15.9	0.89	12.43
17	83.6	0.046	-0.0043	108.7	511.0	57.0	10.4	0.65	14.02
	98.3	0.058	-0.0022	110.4	535.9	80.1	12.3	0.72	12.52
18	65.0	0.037	-0.0035	103.5	523.7	52.4	8.0	0.52	13.88
	78.1	0.047	-0.0019	105.9	541.3	75.4	9.6	0.59	12.66
19	50.9	0.030	-0.0029	98.8	534.5	47.6	6.2	0.41	13.82
	62.9	0.039	-0.0016	101.1	552.7	72.2	7.6	0.49	12.52
20	40.6	0.025	-0.0027	94.6	544.2	38.9	4.8	0.34	13.76
	51.0	0.033	-0.0014	97.0	560.1	67.4	6.0	0.40	12.54

TABLE II: The same as Table I but for $40A$ GeV.

Time	ε^{cell}	ρ_B^{cell}	ρ_S^{cell}	T	μ_B	μ_S	P	s	s/ρ_B^{cell}
fm/c	MeV/fm^3	fm^{-3}	fm^{-3}	MeV	MeV	MeV	MeV/fm^3	fm^{-3}	
9	662.3	0.226	-0.0181	160.2	341.6	75.5	91.8	4.23	18.69
	732.3	0.290	-0.0050	167.2	401.9	105.3	113.5	4.36	15.01
10	492.2	0.175	-0.0145	153.2	354.2	71.6	68.3	3.25	18.60
	524.3	0.219	-0.0041	157.1	417.9	100.4	79.3	3.26	14.85
11	369.4	0.135	-0.0113	146.8	363.7	67.4	51.5	2.53	18.73
	384.5	0.170	-0.0045	148.1	434.5	94.7	56.7	2.48	14.61
12	276.2	0.104	-0.0094	140.5	374.7	62.4	38.7	1.96	18.80
	282.7	0.130	-0.0033	140.0	447.2	90.0	40.9	1.90	14.60
13	205.7	0.081	-0.0075	134.0	390.1	58.0	28.8	1.51	18.66
	211.5	0.101	-0.0030	132.6	460.3	85.0	30.0	1.47	14.53
14	155.6	0.064	-0.0060	128.0	404.0	54.9	21.8	1.18	18.59
	158.4	0.077	-0.0023	126.3	465.9	79.4	22.2	1.15	14.85
15	118.9	0.050	-0.0051	122.3	419.0	50.8	16.6	0.93	18.43
	120.4	0.060	-0.0018	120.5	471.9	74.4	16.8	0.90	15.16
16	90.5	0.040	-0.0041	117.2	426.6	46.3	12.8	0.74	18.81
	93.2	0.047	-0.0013	115.2	479.7	71.2	12.9	0.72	15.38
17	69.9	0.032	-0.0034	112.0	441.0	42.3	9.9	0.59	18.69
	73.8	0.038	-0.0012	110.2	489.8	67.2	10.1	0.59	15.39
18	55.0	0.026	-0.0028	107.0	457.3	39.2	7.6	0.47	18.40
	59.0	0.031	-0.0006	105.7	499.7	70.0	7.9	0.49	15.48
19	43.3	0.021	-0.0025	102.4	469.8	34.2	6.0	0.39	18.34
	47.8	0.026	-0.0006	101.2	512.1	65.7	6.3	0.40	15.31

FIG. 5: (Color online) The total energy density ε versus baryon density ρ_B obtained in the central UrQMD cell of volume (a) $V = 125$ fm^3 and (b) $V = 0.125$ fm^3 during the time evolution of central Au+Au collisions at energies from $11.6A$ GeV to $158A$ GeV. Dashed lines correspond to the non-equilibrium stage of the reaction, solid lines represent the equilibrium phase.

production of hot equilibrated matter with a density of $\rho_B = 1.8 \rho_0$, much higher nuclear densities obtained in microscopic simulations have been reported [27]. One has to bear in mind two important things concerning such density estimates. Firstly, they are very sensitive to the volume of the test-system, especially at the initial stage of the collision. As seen in Fig. 5(a) and Fig. 6(a), the baryon density in 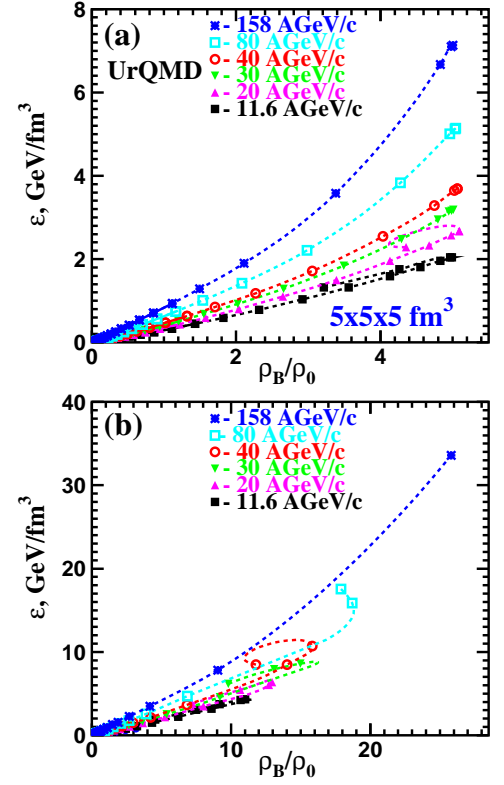both models cannot exceed $5 \rho_0$ in the central cubic cell with volume $V = 5 \times 5 \times 5$ fm^3 regardless of the bombarding energy, while for the smaller cell with volume $V_{small} = 0.5 \times 0.5 \times 0.5$ fm^3 the baryon density can be as high as $20 \rho_0$ in the calculations within the same microscopic models, see Fig. 5(b) and Fig. 6(b). Secondly, such high values of the ρ_B should be treated with great care. The accelerated cold nuclear matter is automatically "compressed" in the calculations by the γ-factor. At the initial stage of a nuclear collision one deals with two opposite fluxes of Lorentz-contracted nucleons which just start to interact with their counterparts. Although the calculated baryon densities are huge, especially for the small cell, this is a purely kinematic effect, since the system is far from local equilibrium. The numbers become meaningful only when the equilibration takes place.

Another interesting effect is the negative (though small) net strangeness density in the cell throughout the evolution of the system depicted in Fig. 7. The result is pretty insensitive to the size of test-volume and can be explained as follows. Strange particles are always produced in pairs, so the net ρ_S is zero. At energies about $40A$ GeV and below kaons emerge predominantly with lambdas and antikaons. Because of the $\bar{s}$-quark in its
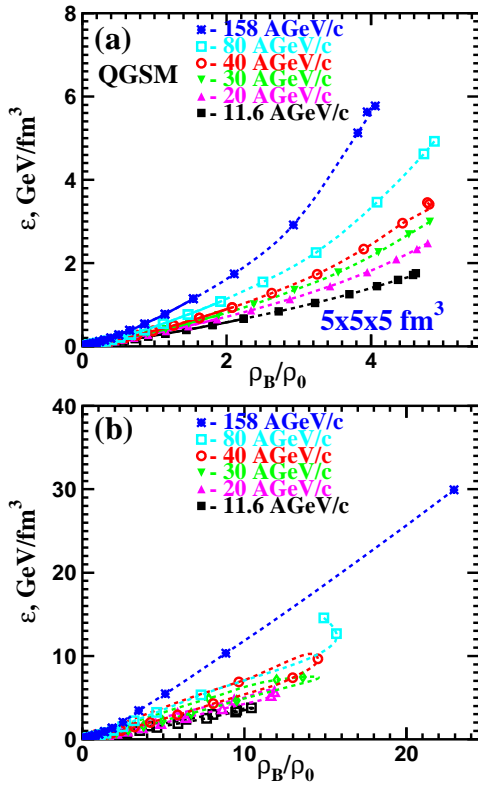
FIG. 6: (Color online) The same as Fig. 5, but for QGSM calculations.

FIG. 7: (Color online) Time evolution of net strangeness density in the central 125 fm^3 cell in (a) UrQMD and (b) QGSM calculations of central Au+Au collisions at energies from 11.6A GeV to 158A GeV. Lines are drawn to guide the eye.

composition, kaons have significantly smaller interaction cross-section with baryons at $p \leq 2\,\mathrm{GeV}/c$ compared to antikaons, which carry the s-quark. Therefore, K leave the central cell with positive net baryon charge easier than Λ or $\overline{K}$ thus resulting to negative net strangeness. At RHIC energies the $B - \overline{B}$ asymmetry in the cell is much less pronounced, and the net ρ_S is very close to zero [7, 11].

Here we distinctly see the role of hadronic degrees of freedom. Despite the net baryon density is about 15% larger in the QGSM calculations than in the UrQMD ones, the absolute value of the net strangeness density is almost 30% higher in the UrQMD cell as compared to that in the QGSM. Extra-strangeness is deposited in the resonance sector, mainly in Λ^* and K^*. Although the net ρ_S in the cell shown in Fig. 7 quickly drops almost to zero after $t = 6\,\mathrm{fm}/c$, its relaxation proceeds slower than that of the net baryon density. Figure 8 displays the instant rise of the ratio $f_s = -\rho_S/\rho_B$ with time t attributed to both microscopic models. The role of the small non-zero net strangeness is not negligible. The difference in particle spectra and, especially, in particle ratios can be about 15% [9] if one performs the SM calculations with essentially zero net strangeness.
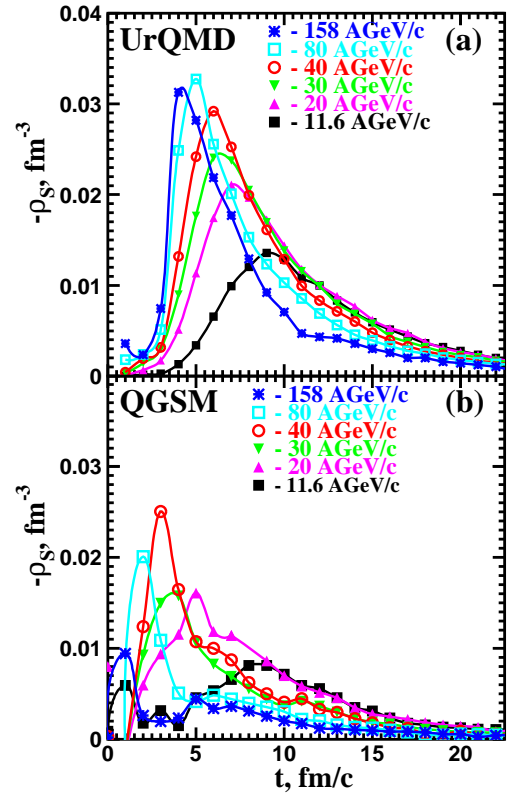
C. EOS in the cell

Isentropic expansion of relativistic fluid is one of the main postulates of Landau hydrodynamic theory [23] of multiparticle production. We cannot prove or disprove this assumption in microscopic simulations for the whole system, simply because a global equilibrium is not attained. Though conditions in the cell are instantly changing, it is possible to check the behavior of the entropy per baryon. Within the 5% accuracy limit, this ratio is nearly conserved in the equilibrium phase of the expansion, see Fig. 9. The entropy densities obtained for the cell in both models are very close to each other, but, because of the difference in net-baryon sector, the ratio s/ρ_B in UrQMD is about 15-20% larger than that in QGSM. Together with the pressure isotropy, the conservation of entropy per baryon supports the application of hydrodynamics.

Any hydrodynamic model relies on the equation of state, which links the pressure of the system to its energy density. Otherwise, the system of hydrodynamic equations is incomplete. The corresponding plot with microscopic pressures $P_{mic}(\varepsilon)$ is presented in Fig. 10, whereas the macroscopic pressures obtained from the SM fit are shown in Fig. 11. In the last plot the dependence of
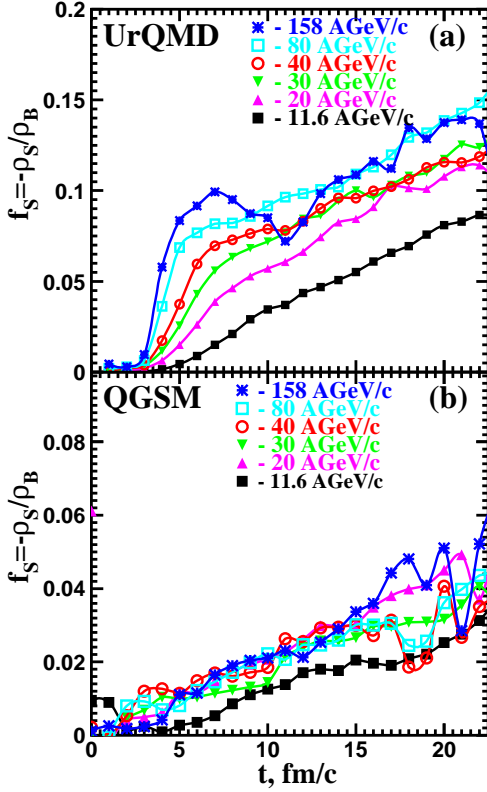
FIG. 8: (Color online) The same as Fig. 7 but for strangeness per baryon, $f_s = -\rho_S/\rho_B$. Lines are drawn to guide the eye.

pressure on energy density is remarkably linear for both models for all energies in question. Thus the EOS has a rather simple form

$$P(\varepsilon) = c_s^2 \varepsilon \ , \qquad (16)$$

where the sonic velocity in the medium $c_s = (dP/d\varepsilon)^{1/2}$ is fully determined by the slopes of the distributions $P(\varepsilon)$. However, if the pressure is determined microscopically and not via the distribution function, the falloff of pressure with decreasing energy density proceeds slightly nonlinearly. This feature can be seen distinctly for top SPS energy in the QGSM calculations. Therefore, for both models we averaged the slopes of the P vs. ε distributions over the whole period of the equilibrated phase (see Fig. 10). It should be noted that due to the averaging over time, respectively energy density, the values do not represent the maximal values for c_s^2 which are reached in the corresponding reactions. They are actually lower, since also energy densities below the critical energy density of about $0.8\,\mathrm{GeV/fm^3}$ contribute to the average.

The extracted values of the c_s^2 are presented in Fig. 12. For the UrQMD calculations the velocity of sound increases from 0.13 at $E_{lab} = 11.6A$ GeV to 0.146 at $E_{lab} = 158A$ GeV, and saturates at $c_s^2 = 0.15$ for RHIC energies, $\sqrt{s} = 130A$ GeV and $\sqrt{s} = 200A$ GeV [11]. In QGSM calculations the averaged sound velocity is about
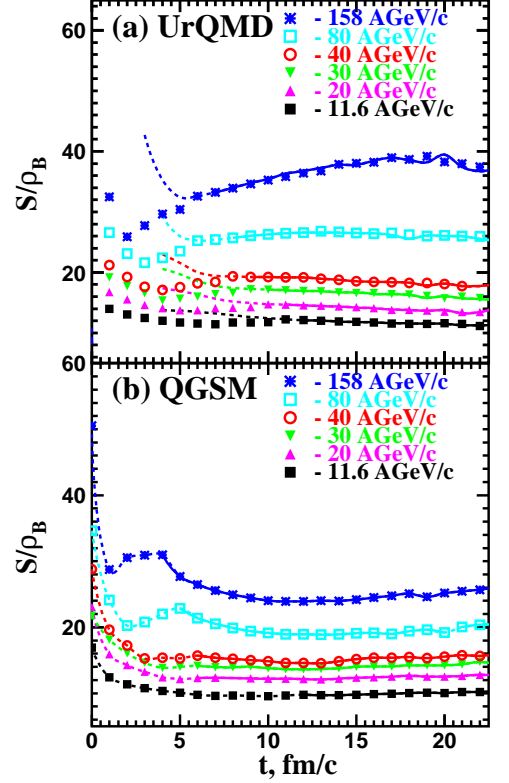

FIG. 9: (Color online) Time evolution of entropy per baryon S/ρ_B in the central 125 fm^3 cell in (a) UrQMD and (b) QGSM calculations of central Au+Au collisions at energies from 11.6A GeV to 158A GeV. Dashed lines correspond to the non-equilibrium stage of the reaction, solid lines represent the equilibrium phase.

0.015 units smaller due to the pion excess. For instance, it reaches $c_s^2 = 0.127$ at $E_{lab} = 40A$ GeV. Both models indicate that at the energy around $E_{lab} = 40A$ GeV the slope of the $c_s^2(\sqrt{s})$ distribution is changing, and the velocity of sound becomes less sensitive to rising bombarding energy.

Let us discuss the obtained values of the c_s^2. For the ultrarelativistic gas of light particles the well-known theoretical result is $c_s = 1/\sqrt{3}$ of the speed of light [28]. As shown in [29], the presence of resonances in particle spectrum generates the decrease of the sonic speed. Employing the empirical dependence [30]

$$\rho(m) \propto m^{\alpha'} \quad (2 \leq \alpha' \leq 3) \ , \qquad (17)$$

where $\rho(m)\,dm$ denotes the number of resonances with masses from m to $m + dm$, one arrives to the equation of state in the form [29]

$$\varepsilon = (\alpha' + 4)\,P \ , \qquad (18)$$

i.e., $\frac{1}{7} \leq c_s^2 \leq \frac{1}{6}$. This trend is reproduced in microscopic models.

Since neither energy density nor pressure can be directly measured in the central area of heavy-ion colli-
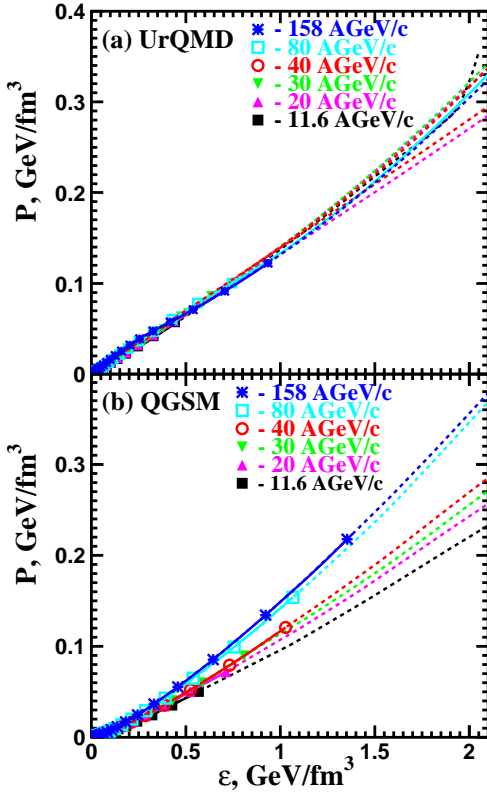
FIG. 10: (Color online) Time evolution of the microscopic pressure P and the energy density ε in the central 125 fm^3 cell in (a) UrQMD and (b) QGSM calculations of central Au+Au collisions at energies from $11.6A$ GeV to $158A$ GeV. Dashed lines correspond to the non-equilibrium stage of the reaction, solid lines represent the equilibrium phase.

FIG. 11: (Color online) The same as Fig. 10 but for macroscopic pressure P extracted from the SM fit to microscopic data.

sions, the experimental evaluation of the c_s is more difficult. One may rely on the hydrodynamic calculations, which claim that the magnitude of the so-called elliptic flow v_2 depends on the speed of sound c_s [31]. Using the estimates, obtained for fixed impact parameter $b = 8$ fm under assumption of constant c_s throughout the system expansion, PHENIX collaboration reported the value $c_s \approx 0.35 \pm 0.05$ [32], i.e. $c_s^2 \approx 0.12 \pm 0.3$, for gold-gold collisions at top RHIC energy $\sqrt{s} = 200A$ GeV. This value is close to our results and also implies rather soft effective EOS.

Lattice calculations [33] predict an asymptotic value of $c_s^2 \sim 0.3$ slightly below the Stefan-Boltzmann limit which indicates the appearance of a strongly coupled partonic medium. Recombination processes decrease the mean free path of the particles and lower thus the viscosity of the medium. By including such processes the sonic speed can be increased above the critical energy density thus coming closer to the lattice predictions [16].

The velocity of sound defines the change of entropy and energy densities with decreasing temperature, provided the local equilibrium is maintained during the expansion. The analytic expressions, which can be derived, e.g., for gas of non-strange mesons with zero chemical potential,
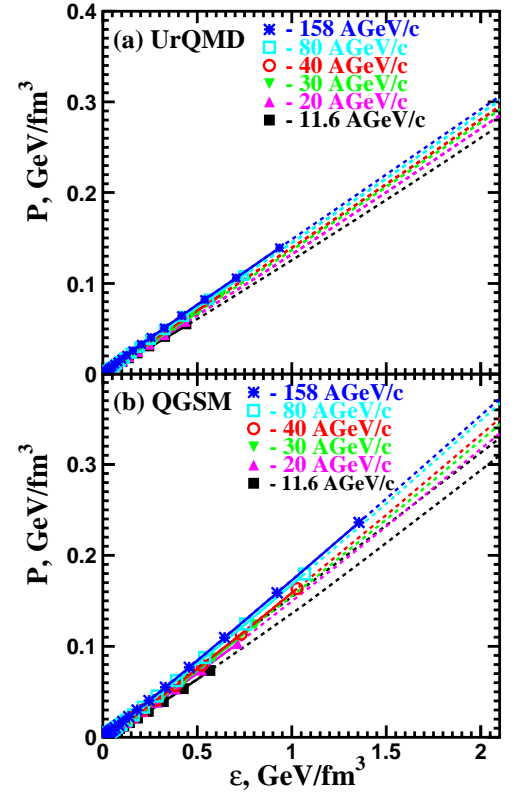
read (see *Appendix* B)

$$\varepsilon = \varepsilon_0 \left(\frac{T}{T_0}\right)^{\frac{1+a}{a}}, \qquad (19)$$

$$s = s_0 \left(\frac{T}{T_0}\right)^{\frac{1}{a}}. \qquad (20)$$

The ratios $\varepsilon/\varepsilon_0$ and s/s_0 as functions of T/T_0 obtained from model calculations at $E_{lab} = 20A$ GeV and $40A$ GeV are plotted in Fig. 13 together with results for $\mu = 0$ given by Eqs. (19)-(20). Although the hadron gas in the cell represents a cocktail of species with different chemical potentials, that can be either zero, positive or negative in case of antiparticles, the curves calculated by the UrQMD and QGSM are not far from the ideal ones. Moreover, there is just a very weak difference between the UrQMD and QGSM curves for both energies. If one formally fits these distributions to Eqs. (19)-(20) using the velocity of sound as fitting parameter, one gets $a = 0.2$ exactly. It would be nice to check whether the deceleration of energy(entropy) density falloff with dropping temperature could be charged solely to the presence of hadrons with non-zero chemical potential. One way to do this is to perform a similar analysis of the cell conditions at RHIC (or higher) energies. - Here strange hadrons, baryons and their resonances are still present [11], but both chemical
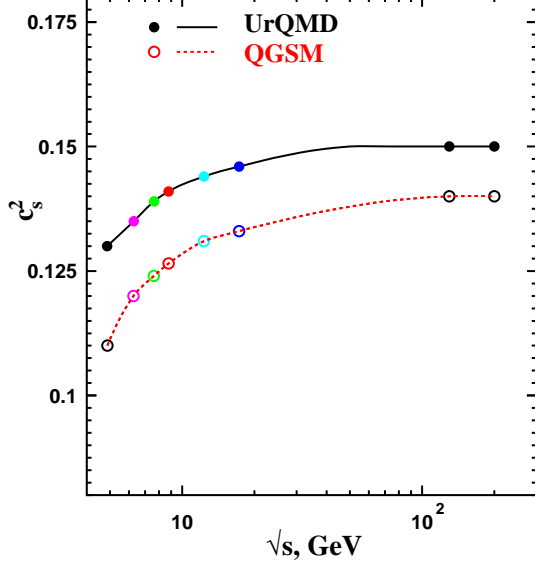
FIG. 12: (Color online) The ratio $P/\varepsilon = c_s^2$, where P is defined microscopically, in the central cell of volume $V = 125\,\text{fm}^3$ as a function of center of mass energy $\sqrt{s}$ in UrQMD (solid symbols) and in QGSM (open symbols) calculations. Lines are drawn to guide the eye.

FIG. 13: (Color online) (a) Ratio of energy densities $\varepsilon/\varepsilon_0$ vs. T/T_0 in the central $V = 125\,\text{fm}^3$ cell. Dashed line and solid line represent UrQMD calculations of central Au+Au collisions at $20A$ GeV and $40A$ GeV, respectively, whereas dotted line and dash-dotted line show the QGSM results for these reactions. Asterisks depict the analytic calculations given by Eqs. (19)-(20) with $\mu = 0$ and $a = c_s^2 = 0.14$. (b) The same as (a) but for the ratio of entropy densities s/s_0.

potentials, μ_B and μ_S, are quite small. Therefore, one may expect that the microscopic results would be closer to those presented by Eqs. (19)-(20).

Note also, that pressure in the cell changes with energy density quite smoothly, and no peculiarities which can be attributed to first-order phase transition are seen in the early stage of the reaction. - Here we simply extend the formalism of extraction of the thermodynamic parameters to the non-equilibrium phase, where one cannot trust the obtained values anymore. This was done merely in order to find any traces of the transition related to the onset of equilibrium and to changes of the effective EOS in the models. However, the analysis is performed for the fixed cubic cell of relatively large volume $V = 125$ fm^3, where the matter is distributed non-homogeneously at early times. To get rid of the evident ambiguities, the scheme is properly modified.

D. Early stage of the evolution

The central cell is further subdivided into the smaller ones, embedded one into another. The size of the initial test-volume is just $V_{init} = 0.125$ fm^3, and the energy density ε of the cells becomes the main parameter now. If the ε of the inner cell is not the same (within the 5% limit of accuracy) as the energy density of the outer one, the SM analysis of the thermodynamic conditions is performed for the inner cell. If the energy density is uniformly dis-
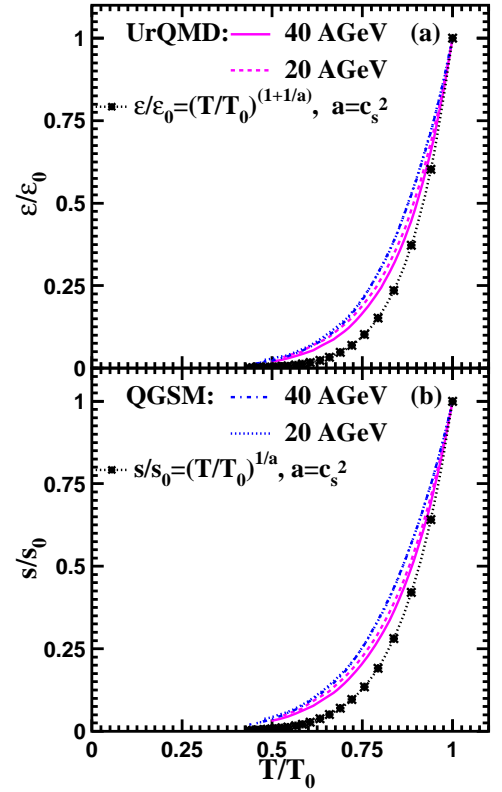
tributed within the outer cell, the latter becomes a new test-volume, and so on. In the latter case it appears (see Fig. 9) that the onset of the isentropic expansion regime in the central area occurs significantly earlier than the formation of equilibrated matter. Moreover, at the collision energies below $80A$ GeV entropy per baryon ratio seems to be quite stable almost from the beginning of the reaction.

Evolutions of the temperature and baryon chemical potential both in the central cell of the fixed volume $V = 125\,\text{fm}^3$ and in the expanding energy area are depicted in Fig. 14. One sees

that the transition to equilibrium proceeds quite smoothly if the analysis is performed for the fixed cell (Fig. 14, upper plot). In contrast, in the area with uniformly distributed energy the transition to the equilibrated phase is characterized by a kink distinctly seen in each of the phase diagrams in both microscopic models. Although this effect takes place along the lines of the constant entropy per baryon, it should not be automatically linked to the highly anticipated quark-hadron phase transition. The reason is simple, - extraction of
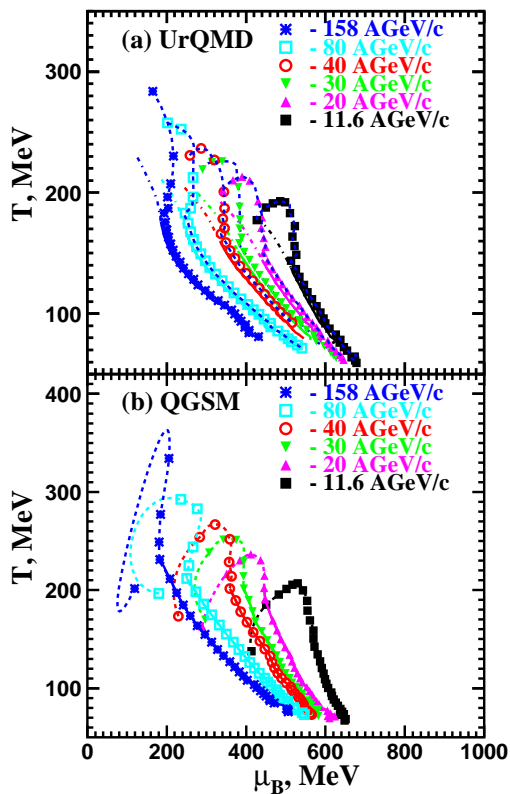
FIG. 14: (Color online) The evolution of the temperature T and baryon chemical potential μ_B in the central cell of central Au+Au collisions at energies from $11.6A$ GeV to $158A$ GeV. Both parameters are extracted from the fit to the SM. Symbols and dashed lines show the evolution of these quantities in a cell of instantly increasing volume ($V_{init} = 0.125\,\mathrm{fm}^3$), while dash-dotted (upper plot) and full (both plots) lines are related to calculations with the fixed volume $V = 125\,\mathrm{fm}^3$.

the thermodynamic parameters, such as T, P, μ_B and μ_S (but not the entropy density, which is determined microscopically), by means of the equilibrium statistical model is doubtful for the non-equilibrium phase. On the other hand, the formation of the kink may not be accidental. It is correlated with the significant reduction of the number of processes going via the formation and fragmentation of strings, and, therefore, with the inelastic (chemical) freeze-out of particles. - In both models the matter, produced in a central area in central heavy-ion collisions at energies between AGS and SPS, is dominated by (pseudo)elastic collisions after $t \approx 6 \div 8$ fm/c [34, 35, 36]. - In the fixed-cell analysis all parameters within the cell are averaged and the transition is smeared out. The observed phenomenon can easily mimic the signature of the QCD phase transition in the T-μ_B plane, found in lattice QCD calculations [37] also along the lines of the constant entropy per baryon.

Figure 14 demonstrates also that thermodynamic characteristics of the fixed-size cell and the instantly growing energy-homogeneous area coincide completely during the equilibrium stage. In accord with earlier observation [10],

neither the mechanical reduction of the test-volume in longitudinal direction nor the criterion of uniformly distributed energy density alone can help us in searching for quick equilibration in the central zone of relativistic heavy-ion collisions. Criteria of local thermal and chemical equilibrium described in Sect. IV are fulfilled after the chemical freeze-out in the test-volume, when the production of new particles in the system is ceased.

VI. CONCLUSIONS

In summary, two different microscopic string models were used to study the formation and evolution of the locally equilibrated matter in the central zone of heavy-ion collisions at energies from $11.6A$ GeV to $160A$ GeV. Calculations were performed both for the cubic central cell of fixed volume $V = 125$ fm^3 and for the instantly expanding area of homogeneous energy density. Traditional approach based on the fulfillment of the conditions of kinetic, thermal and chemical equilibrium has been applied to decide whether or not the equilibrium is reached. Both models favor the formation of the equilibrated matter for a period of about 10 fm/c. During this period the expansion of matter in the central cell proceeds isentropically with constant entropy per baryon. The equation of state can be approximated by a simple linear dependence $P = a(\sqrt{s})\varepsilon$, where the square of the speed of sound $c_s^2 = a(\sqrt{s})$ varies from 0.13 (AGS) to 0.15 (SPS) in the UrQMD calculations, and from 0.11 (AGS) to 0.14 (SPS) in the QGSM ones. In both models the rise of $a(\sqrt{s})$ with energy is slowed down after $E_{lab} = 40A$ GeV and saturates at RHIC energies. This change is assigned to the transition from baryon-dominated to meson-dominated matter.

Study of the expanding area of the isotropically distributed energy reveals that the relaxation to equilibrium in this dynamic region proceeds at the same rate as in the case of the fixed-size cell. However, the entropy per baryon ratio becomes constant before the state of equilibrium is attained. Here both microscopic models unambiguously show the presence of a kink in the T-μ_B phase diagrams. The higher the collision energy, the earlier the kink formation. Its origin is linked to the freeze-out of inelastic reactions in the considered area.

APPENDIX A: REDUCTION OF TEMPERATURE

Let us consider non-relativistic ideal hadron gas which contains non-equilibrium number of pions, while the other hadron species correspond to their equilibrium values. In thermal equilibrium the total energy of the gas is a sum of the masses of all particles (potential term) and the energies of their thermal motion (kinetic term). Compared to the case of fully equilibrized hadron gas, the temperature of the system with overpopulated amount of pions should reduce so that the total energies of both systems remain the same.

One can write

$$E^{(1)} = E^{(2)} , \tag{A1}$$

$$E^{(1)} = \sum_i m_i^{(1)} N_i^{(1)} + \frac{3}{2} T^{(1)} \sum_i N_i^{(1)} , \tag{A2}$$

$$E^{(2)} = \sum_i m_i^{(2)} N_i^{(2)} + \frac{3}{2} T^{(2)} \sum_i N_i^{(2)} , \tag{A3}$$

$$N_\pi^{(1)} = \alpha N_\pi^{(2)} , \tag{A4}$$

$$N_{i\neq\pi}^{(1)} = N_{i\neq\pi}^{(2)} , \tag{A5}$$

where the superscripts (1) and (2) are related to partially non-balanced (w.r.t. pions) and fully equilibrized system, respectively. Parameter $\alpha > 1$ measures the excess of pions in system (1). From Eqs. (A1)-(A5) we have

$$m_\pi N_\pi^{(2)} = \frac{3}{2} \left[(T^{(2)} - T^{(1)} \sum_i N_i^{(2)} - (\alpha - 1) T^{(1)} N_\pi^{(2)} \right] \tag{A6}$$

Introducing the reduced variables

$$\beta = \sum_i N_i^{(2)} / N_\pi^{(2)} , \quad (\beta > 1) \tag{A7}$$

$$\gamma = T^{(1)}/T^{(2)} , \quad (0 < \gamma < 1) \tag{A8}$$

$$\delta = \frac{2}{3} \frac{m_\pi}{T^{(2)}} , \tag{A9}$$

we get finally

$$\beta(1 - \gamma) = (\alpha - 1)(\gamma + \delta) \tag{A10}$$

Now knowing the pion abundance in particle spectrum β^{-1} at chemical equilibrium and pion excess α one can estimate the drop of temperature γ in the system due to re-distribution of kinetic energy among the extra degrees of freedom.

APPENDIX B: EVOLUTION OF ε AND s WITH T AT $\mu = 0$

Gibbs free energy G is linked to energy E and entropy S of the system with pressure P, volume V and temperature T via the equality

$$G = E + PV - TS . \tag{B1}$$

On the other hand, $G = \mu N$, where μ is the chemical potential and N is the number of particles. If the chemical potential is absent, Eq. (B1) is reduced to the following expression for the energy and entropy densities, $\varepsilon = E/V$ and $s = S/V$, respectively:

$$\varepsilon + P = Ts \tag{B2}$$

Utilizing the condition $\mu = 0$, one can derive from basic thermodynamic equalities [28]

$$d\varepsilon = T\,ds , \tag{B3}$$

$$dP = s\,dT . \tag{B4}$$

Inserting the equation of state $dP = a\,d\varepsilon$ into these equations, we get after straightforward calculations

$$\frac{a}{1+a} \frac{d\varepsilon}{\varepsilon} = \frac{dT}{T} , \tag{B5}$$

$$a \frac{ds}{s} = \frac{dT}{T} , \tag{B6}$$

and, finally,

$$\frac{\varepsilon}{\varepsilon_0} = \left(\frac{T}{T_0} \right)^{\frac{1+a}{a}} , \tag{B7}$$

$$\frac{s}{s_0} = \left(\frac{T}{T_0} \right)^{\frac{1}{a}} . \tag{B8}$$

The obtained results are general for particles with $\mu = 0$ and do not depend on the expansion, e.g. longitudinal or spherical, scenario.

[1] W. Henning, Nucl. Phys. **A734**, 654 (2004).
[2] M.A. Stephanov, K. Rajagopal, E.V. Shuryak, Phys. Rev. Lett. **81**, 4816 (1998).
[3] Z. Fodor and S.D. Katz, JHEP **0404**, 050 (2004).
[4] S. Ejiri, C.R. Allton, S.J. Hands, O. Kaczmarek, F. Karsch, E. Laermann, and C. Schmidt, Prog. Theor. Phys. Suppl. **153**, 118 (2004).
[5] J. Cleymans and K. Redlich, Phys. Rev. C **60**, 054908 (1999).
[6] A. Andronic, P. Braun-Munzinger, and J. Stachel, Nucl.

Phys. **A772**, 167 (2006).

[7] Z.D. Lu, A. Faessler, C. Fuchs, and E.E. Zabrodin, Phys. Rev. C **66**, 044905 (2002); J. Phys. G **28**, 2127 (2002).

[8] L.V. Bravina, M.I. Gorenstein, M. Belkacem, S.A. Bass, M. Bleicher, M. Brandstetter, M. Hofmann, S. Soff, C. Spieles, H. Weber, H. Stöcker, and W. Greiner, Phys. Lett. B **434**, 379 (1998).

[9] L.V. Bravina, E.E. Zabrodin, M.I. Gorenstein, S.A. Bass, M. Belkacem, M. Bleicher, M. Brandstetter, C. Ernst, M. Hofmann, L. Neise, S. Soff, H. Weber, H. Stöcker, and W. Greiner, Phys. Rev. C **60**, 024904 (1999).

[10] L.V. Bravina, M. Brandstetter, M.I. Gorenstein, E.E. Zabrodin, M. Belkacem, M. Bleicher, S.A. Bass, C. Ernst, M. Hofmann, S. Soff, H. Stöcker, and W. Greiner, J. Phys. G **25**, 351 (1999); L.V. Bravina, E.E. Zabrodin, M.I. Gorenstein, S.A. Bass, M. Belkacem, M. Bleicher, M. Brandstetter, C. Ernst, Amand Faessler, W. Greiner, S. Soff, H. Stöcker, and H. Weber, Nucl. Phys. **A661**, 600c (1999).

[11] L.V. Bravina, E.E. Zabrodin, S.A. Bass, M. Bleicher, M. Brandstetter, Amand Faessler, C. Fuchs, W. Greiner, S. Soff, and H. Stöcker, Phys. Rev. C **63**, 064902 (2001); L.V. Bravina, E.E. Zabrodin, S.A. Bass, Amand Faessler, C. Fuchs, M.I. Gorenstein, W. Greiner, S. Soff, H. Stöcker, and H. Weber, Nucl. Phys. **A698**, 383c (2002); L.V. Bravina, E.E. Zabrodin, S.A. Bass, M. Bleicher, M. Brandstetter, Amand Faessler, C. Fuchs, M.I. Gorenstein, W. Greiner, S. Soff, and H. Stöcker, J. Phys. G **27**, 421 (2001).

[12] L.V. Bravina, I. Arsene, M.S. Nilsson, K. Tywoniuk, and E.E. Zabrodin, J. Phys. G. **32**, S213 (2006); L.V. Bravina, I. Arsene, M.S. Nilsson, K. Tywoniuk, E.E. Zabrodin, M. Bleicher, H. Stöcker, and W. Greiner, Int. J. Mod. Phys. E **16**, 777 (2007).

[13] S.A. Bass, M. Belkacem, M. Bleicher, M. Brandstetter, L. Bravina, C. Ernst, L. Gerland, M. Hofmann, S. Hofmann, J. Konopka, G. Mao, L. Neise, S. Soff, C. Spieles, H. Weber, L.A. Winckelmann, H. Stöcker, W. Greiner, C. Hartnack, J. Aichelin, and N. Amelin, Prog. Part. Nucl. Phys. **41**, 255 (1998); M. Bleicher, E. Zabrodin, C. Spieles, S.A. Bass, C. Ernst, S. Soff, L. Bravina, M. Belkacem, H. Weber, H. Stöcker, and W. Greiner, J. Phys. G **25**, 1859 (1999).

[14] N.S. Amelin and L.V. Bravina, Sov. J. Nucl. Phys. **51**, 133 (1990) [Yad. Fiz. **51**, 211 (1990)]; N.S. Amelin, L.V. Bravina, L.P. Csernai, V.D. Toneev, K.K. Gudima, and S.Yu. Sivoklokov, Phys. Rev. C **47**, 2299 (1993).

[15] J. Bleibel, G. Burau, Amand Faessler, and C. Fuchs, Nucl. Phys. **A767**, 218 (2006).

[16] J. Bleibel, G. Burau, Amand Faessler, and C. Fuchs, Phys. Rev. C **76**, 024912 (2007); J. Bleibel, G. Burau,

and C. Fuchs, Phys. Lett. B **659**, 520 (2008).

[17] B. Andersson, G. Gustafson, and B. Nilsson-Almqvist, Nucl. Phys. B **281**, 289 (1987).

[18] V. Gribov, Sov. Phys. JETP **26**, 414 (1968) [Zh. Eksp. Theor. Fiz. **53**, 654 (1967)]; L.V. Gribov, E.M. Levin, and M.G. Ryskin, Phys. Rep. **100**, 1 (1983).

[19] C. Pajares and Yu.M. Shabelski, *Relativistic Nuclear Interactions* (URSS, Moscow, 2007); A.B. Kaidalov, Surveys in High Energy Phys. **13**, 265 (1999).

[20] T. Sjöstrand, Comp. Phys. Comm. **39**, 347 (1986).

[21] R.D. Field and R.P. Feynman, Nucl. Phys. B **136**, 1 (1978).

[22] E. Fermi, Prog. Theor. Phys. **5**, 570 (1950).

[23] L.D. Landau, Izv. Akad. Nauk SSSR, Ser. Fiz. **17**, 51 (1953) (in Russian); S.Z. Belenkij and L.D. Landau, Nuovo Cimento Suppl. **3**, 15 (1956).

[24] M. Berenguer, C. Hartnack, G. Peilert, H. Stöcker, W. Greiner, J. Aichelin, and A. Rosenhauer, J. Phys. G **18**, 655 (1992).

[25] M. Belkacem, M. Brandstetter, S.A. Bass, M. Bleicher, L. Bravina, M.I. Gorenstein, J. Konopka, L. Neise, C. Spieles, S. Soff, H. Weber, H. Stöcker, and W. Greiner, Phys. Rev. C **58**, 1727 (1998).

[26] L.V. Bravina, E.E. Zabrodin, S.A. Bass, M. Bleicher, M. Brandstetter, S. Soff, H. Stöcker, and W. Greiner, Phys. Rev. C **62**, 064906 (2000).

[27] I.C. Arsene, L.V. Bravina, W. Cassing, Yu.B. Ivanov, A. Larionov, J. Randrup, V.N. Russkikh, V.D. Toneev, G. Zeeb, and D. Zschiesche, Phys. Rev. C **75**, 034902 (2007).

[28] L.D. Landau and E.M. Lifshitz, *Statistical Physics* (Pergamon, Oxford, 1980).

[29] E. Shuryak, Sov. J. Nucl. Phys. **16**, 395 (1973) [Yad. Fiz. **16**, 707 (1972)].

[30] R. Hagedorn, Nuovo Cimento Suppl. **3**, 147 (1965).

[31] R. S. Bhalerao, J.-P. Blaizot, N. Borghini, and J.-Y. Ollitrault, Phys. Lett. B **627**, 49 (2005).

[32] A. Adare *et al.* (PHENIX Collaboration), Phys. Rev. Lett. **98**, 162301 (2007).

[33] Y. Aoki, Z. Fodor, S. D. Katz and K. K. Szabo, JHEP **0601**, 089 (2006).

[34] M. Bleicher and J. Aichelin, Phys. Lett. B **530**, 81 (2002).

[35] L.V. Bravina, I.N. Mishustin, N.S. Amelin, J.P. Bondorf, and L.P. Csernai, Phys. Lett. B **354**, 196 (1995).

[36] L.V. Bravina, I.N. Mishustin, J.P. Bondorf, Amand Faessler, and E.E. Zabrodin, Phys. Rev. C **60**, 044905 (1999).

[37] S. Ejiri, F. Karsch, E. Laermann, and C. Schmidt, Phys. Rev. D **73**, 054506 (2006).